Lattice Boltzmann approaches to the Euler-Euler equations for two-phase flows

Githin Tom Zachariah* and Harry E. A. Van den Akker
Synthesis and Solid State Pharmaceutical Centre (SSPC), University of Limerick, Limerick V94 T9PX, Ireland and Bernal Institute, University of Limerick, Limerick V94 T9PX, Ireland

(Received 9 January 2025; accepted 22 December 2025; published 6 April 2026)

This paper reports on the development of a lattice Boltzmann (LB) code for the Euler-Euler, or two-fluid, large eddy simulation (LES) of turbulent dispersed two-phase flow. To correct for the inbuilt pressure handling inherent to the standard LB method, we develop two LB approaches to the Euler-Euler equations. In the first approach, we naturally remove the inbuilt pressure component by invoking the well-balanced LB method proposed by Guo *et al.* [Phys. Fluids **33**, 031709 (2021)]. Subsequently, the correct pressure term is added as an external force in a Poisson equation. The second approach utilizes a mixture model to generate the required pressure field, assuming an incompressible dilute mixture. This is then coupled to an LB equation for the dispersed phase flow. The two proposed models are validated against two test cases: a falling cloud of particles and a Rayleigh-Taylor instability. The results demonstrate the accuracy of the proposed models while identifying their differences. Subsequently, both models are used to simulate a homogeneous isotropic turbulent two-phase emulsion in a LES supported by the static Smagorinsky subgridscale model. The results of these LESs are compared with a full-scale direct numerical simulation solution. The new models reproduce the larger scales of turbulence accurately, demonstrating the robustness and accuracy of the two proposed models in complex and chaotic scenarios.

DOI: 10.1103/b4mq-2hm6

I. INTRODUCTION

Multiphase flows are widespread in industrial processes and often involve high levels of turbulence. Turbulent multiphase flows are characterized by a wide range of scales of interaction between the phases. At smaller scales, the interaction between the phases at their phase interfaces can lead to complex behavior that is hard to describe and simulate, particularly when the two phases are fluids and the interfaces are deformable. The effects of these small-scale processes often propagate into larger scales, which are much easier to observe under experimental conditions. This has inspired the development of direct numerical simulation (DNS) techniques to precisely simulate the interaction between turbulence and phase interfaces and its effects on large-scale behavior which can be experimentally measured. However, due to the large sizes of equipment in industrial processes of interest, simulations that resolve such phase interfaces while simultaneously solving for the largest scales of fluid motion are currently infeasible.

*Contact author: githintz@gmail.com

Published by the American Physical Society under the terms of the Creative Commons Attribution 4.0 International license. Further distribution of this work must maintain attribution to the author(s) and the published article's title, journal citation, and DOI.

This distinction in scales already plays a role in turbulent single-phase flows, for which various methods have been developed to simulate the overall flow while modeling the small-scale effects by using various approximations and empirical relations. The effects of small-scale turbulence can be modeled [1], by using either a Reynolds-averaged Navier-Stokes (RANS) approach or a large eddy simulation (LES) technique. RANS models utilize time-averaging to isolate and resolve the averaged flow by invoking a turbulence model to represent the effect of all turbulent eddies. Various turbulence models such as the $k-\epsilon$ and $k-\omega$ SST models have been developed, each with their own advantages and disadvantages. RANS models are widely used in industrial applications due to their low computational cost. However, LES is known to be more accurate since it resolves most of the scales of flow and uses a subgrid-scale (SGS) model to approximate the effect of the smallest scales only. With rapid advances in computational power, LESs are becoming increasingly accessible to large-scale problems. Therefore, in this study, we focus on LESs.

Particularly for the transient LESs and DNSs, the lattice Boltzmann (LB) method has emerged as an accurate and fast alternative to finite volume (FV) solvers. It solves the LB equation, which models the evolution of a distribution function. The moments of this distribution function can be used to derive relevant macroscopic variables such as pressure and momentum. Further details on its implementation are given in Sec. II B. Using a Chapman-Enskog expansion, the Navier-Stokes equation can be derived from the LB equation [2]. The main advantage of LB lies in its simple and efficient parallel implementation. After the initial exploratory study by Eggels (1996) [3], Derksen and Van den Akker reported in a suite of papers on the use of LESs in, among other applications, stirred vessels and cyclones, starting with their 1999 paper [4]. Hartmann *et al.* [5] reported that their LB LES code reproduced the turbulent flow in a stirred vessel better than a FV RANS-based code. Currently, the commercial code M-Star, based on their work, is available for simulating turbulent flows in stirred vessels. The question now is whether LB can also be made suitable for simulating dispersed two-phase flows.

A. Multiphase modeling

The presence of an additional phase has a significant effect on the local flow fields of the carrier phase, particularly in the case of deformable drops and bubbles. The interaction between the phases has to be accounted for in addition to the (small-scale) turbulence, such as already proposed by Sato and Sekoguchi [6]. Based on the approach used to simulate the behavior of the dispersed phase, multiphase simulations can be classified (see, e.g., Van den Akker [7]) into two types: Euler-Lagrange (E-L) [8–10] and Euler-Euler (E-E) [11,12].

E-L methods treat the dispersed phase as a collection of Lagrangian particles. The motion of each of these Lagrangian particles is tracked and their interaction with the surrounding Eulerian fluid is modeled. E-L models often use a point-particle approach, which assumes that the particles are smaller than the grid spacing. In addition, the flow field around the particles is not resolved. Particle-particle collision models can be used to enhance the accuracy of E-L models. Although this type of model can generate accurate results, it is restricted to use with dilute systems, i.e., systems with low dispersed phase volume fraction [13]. At higher volume fractions, the huge number of Lagrangian particles required not only becomes computationally prohibitive but physically stands more or less for a porous medium, which contradicts the point-particle approximation. Currently, the LB based M-Star software provides the option for Lagrangian particle tracking.

The E-E method is a more affordable alternative that has been widely used in industrial applications. It involves treating the dispersed phase as a continuum via the two-fluid equations and modeling of the phase interactions by means of various models. This approach enables the use of existing Eulerian FV-based solvers to simulate the two phases separately. Several authors, such as Mudde and Van den Akker [14], Oey *et al.* [15,16] and Jamshidian *et al.* [17,18] solved various RANS-based two-fluid models to simulate various turbulent bubbly flows. Deen *et al.* [19], Niceno *et al.* [20], Ma *et al.* [21] and Fard *et al.* [22] reported on E-E LESs of bubbly flows. Dhotre *et al.* [23] and Papoulias *et al.* [24] compared the RANS approach and the LES technique for solving

two-fluid equations for turbulent bubble columns. Turbulence in such gas-liquid systems is much more complicated than in single-phase flows and has been the subject of several SGS modeling studies—see, e.g., Van den Akker [25], and Long *et al.* [26,27]. Although for dilute systems the E-E approach may be less accurate than an E-L approach, its versatility enables its use in a wide range of flow conditions. Usually, the E-E equations are solved by using the traditional FV method. The challenge addressed in this paper is the development of an LB LES tool for an E-E set of turbulent-flow equations.

B. Current study

One of the key advantages of LB is its inbuilt pressure handling, which does not require the use of an iterative pressure Poisson solver. This is achieved by assuming a weakly compressible fluid along with the ideal gas equation that relates the local density to the local pressure. However, this approach makes it difficult to realize the E-E equations, since all phases need to share a common pressure field. Various studies have suggested possible strategies to solve this issue. Most of the proposed solutions add a correction term directly or indirectly to cancel the erroneous part of the inbuilt pressure term [28–31]. Another approach uses the nonconservative form of the E-E equations along with mass and momentum source terms to arrive at the correct E-E equations. Both of these methods have been shown to lack accuracy and robustness [28].

This work introduces two new approaches to designing a suitable E-E model based on the LB framework. In the first approach, we make use of a pressure-free variant of LB [32] to remove any inbuilt pressure effects and introduce the pressure as an external force. Following the approach of [33,34], a pressure Poisson equation is solved to ensure a divergence-free mixture velocity. In the second approach, the E-E equations are added to obtain a two-phase mixture equation [34,35]. This equation is then solved by using an incompressible LB method while a pressure-free LB method is used to model the dynamics of the dispersed phase. Both approaches are shown to result in suitable E-E equations (with minor approximations only), while preserving stability to simulate turbulent flows in the LES approach.

This paper is organized as follows. Section II describes the methodology used and the proposed models. We first begin by defining the target E-E equations and the standard form of LB. Subsequently, we modify the standard model to obtain a pressure-free LB. We then introduce the two new methods for reintroducing the pressure effects and thus obtain the correct E-E equations. With the ultimate goal of developing an E-E LES model in LB for turbulent multiphase flows, Sec. III validates the model against two standard test cases: A falling swarm of particles, Rayleigh-Taylor instability. Subsequently, the models are used for an LES of homogeneous isotropic turbulence in Sec. IV. The observations from these test cases are then aggregated and the conclusions are presented in Sec. V.

II. METHODOLOGY

A. Target equations: E-E Navier-Stokes

The target of this study, the E-E model, approximates the dispersed phase as a continuum and models its behavior with the help of a Navier-Stokes (NS) equation. The resultant set of equations for the two phases is given as

$$\frac{\partial \rho_k \alpha_k}{\partial t} + \nabla \rho_k \alpha_k \boldsymbol{u}_k = 0, \tag{1}$$

$$\frac{\partial (\rho_k \alpha_k \boldsymbol{u}_k)}{\partial t} + \nabla \cdot (\rho_k \alpha_k \boldsymbol{u}_k \boldsymbol{u}_k) = -\alpha_k \nabla P + \nabla \cdot \left[\mu_k \alpha_k \left(\nabla \boldsymbol{u}_k + \nabla \boldsymbol{u}_k^T\right)\right] + \rho_k \alpha_k \boldsymbol{g} + \boldsymbol{F}_{D,k}, \tag{2}$$

where subscript k denotes the phase, ρ is density, $\boldsymbol{u}$ is the velocity vector, α stands for volume fraction, μ for dynamic viscosity, $\mathbf{g}$ is the acceleration due to gravity, and $\boldsymbol{F}_{D,k}$ contains the interphase momentum transfer terms (only drag force in this study), and g is the acceleration due

to gravity. The volume fractions of the two components are related by $\sum \alpha_k = 1$. The momentum equations for each phase are coupled through a common pressure field and by interphase momentum transfer.

B. Standard lattice Boltzmann method

Given the above target equations, the standard LB equation (LBE) need to be modified to correctly incorporate the phase volume fractions within its constituent terms. The LBE describes the evolution of a distribution function (f), the moments of which are related to relevant macroscopic properties such as density and velocity. This distribution is normally discretized in space along uniformly distributed lattices in d dimensions and is restricted to q discrete directions. Based on the number of dimensions and allowed directions, the resulting scheme is denoted as DdQq scheme. Here we use the $D3Q19$ scheme which provides a good balance between accuracy and cost.

The governing LBE for the distribution function is given as

$$f_i(\mathbf{x} + \mathbf{c}_i \Delta t, t + \Delta t) - f_i(\mathbf{x}, t) = -\frac{\Delta t}{\tau}\big(f_i(\mathbf{x}, t) - f_i^{\mathrm{eq}}(\mathbf{x}, t)\big), \tag{3}$$

where Δt is the time step (set to 1 in LB), $\mathbf{c}_i$ are the velocity components in the various lattice directions i, and τ is the relaxation time that is used to set the kinematic viscosity $\nu = c_s^2(\tau - 0.5\Delta t)$. Here, c_s is the speed of sound, which equals $1/\sqrt{3}$ for the $D3Q19$ lattice. The right-hand side of the equation constitutes the BGK collision operator [36] which relaxes the distribution function toward an equilibrium distribution (f_i^{eq}) given by

$$f_i^{\mathrm{eq}} = w_i \rho \left(1 + \frac{\boldsymbol{c}_i \cdot \boldsymbol{u}^{\mathrm{eq}}}{c_s^2} + \frac{(\boldsymbol{c}_i \cdot \boldsymbol{u}^{\mathrm{eq}})^2}{2c_s^4} - \frac{\boldsymbol{u}^{\mathrm{eq}} \cdot \boldsymbol{u}^{\mathrm{eq}}}{2c_s^2}\right), \tag{4}$$

where w_i is a weight determined by the discretization scheme, ρ is the fluid density, and the superscript eq denotes equilibrium quantities. Finally, the macroscopic variables can be derived from the moments of the distribution function as

$$\sum_i f_i = \rho, \quad \sum_i \boldsymbol{c}_i f_i = \rho \boldsymbol{u}. \tag{5}$$

The pressure can be derived from the density as $P = c_s^2 \rho$, making the standard LB weakly compressible.

Numerous techniques have been developed to incorporate external forces in LB [37]. Generally, these methods shift the equilibrium velocity and/or add an additional source term to the LB equation. Unless mentioned otherwise, we use the Shan and Chen approach which involves redefining the equilibrium velocity without adding any source terms [38]. Using this approach, the equilibrium velocity can now be defined as

$$\boldsymbol{u}^{\mathrm{eq}} = \boldsymbol{u} + \frac{\boldsymbol{F}\tau}{\rho}, \tag{6}$$

where $\boldsymbol{F}$ contains all external forces. The polynomial form of these equations makes its implementation simpler and faster than traditional FV solvers, albeit at a higher memory requirement. The solution to the LBE involves two steps: streaming, and collision. The streaming step involves the advection of the distribution function to neighboring lattices, and the collision step relaxes the advected distribution function following the BGK operator. The local and nonlocal parts of the equation (the collision and streaming steps, respectively) are hence decoupled, making parallelization relatively simple.

By using a Chapman-Enskog expansion [2], this set of equations can be shown to converge to the correct single-phase Navier-Stokes equations:

$$\frac{\partial(\rho \boldsymbol{u})}{\partial t} + \boldsymbol{\nabla} \cdot (\rho \boldsymbol{u}\boldsymbol{u}) = -\boldsymbol{\nabla} P + \boldsymbol{\nabla} \cdot [\mu(\boldsymbol{\nabla}\boldsymbol{u} + (\boldsymbol{\nabla}\boldsymbol{u})^T)] + \boldsymbol{F}. \tag{7}$$

The (standard) LB method presumes a direct relation between pressure and density instead of the FV approach of solving the pressure field iteratively with the help of a Poisson equation (actually a pressure correction equation derived from the continuity equation). However, this feature is only valid when the fluid is incompressible and breaks down in the case of multiple interpenetrating phases. We therefore come up with two options to arrive at a divergence-free velocity field for multiphase flows.

The first (common) step to achieving our proposed models is taken by modifying the zeroth moment of the LB equation to account for the local volume fractions of the phases. Herein, the dispersed phase is denoted by a subscript d and the continuous phase by a subscript c. The newly modified zeroth- and first-order moments for the dispersed and continuous phases become

$$\sum_i f_{i,d}^{\mathrm{eq}} = \alpha_d \rho_d, \tag{8}$$

$$\sum_i f_{i,c}^{\mathrm{eq}} = \alpha_c \rho_c, \tag{9}$$

$$\sum_i \boldsymbol{c}_i f_{i,d}^{\mathrm{eq}} = \alpha_d \rho_d \boldsymbol{u}_d, \tag{10}$$

$$\sum_i \boldsymbol{c}_i f_{i,c}^{\mathrm{eq}} = \alpha_c \rho_c \boldsymbol{u}_c, \tag{11}$$

$$\alpha_c + \alpha_d = 1, \tag{12}$$

where α_d and α_c are the volume fractions of the dispersed phase and the continuous phase, respectively. This modifies the resultant Navier-Stokes equations as

$$\frac{\partial(\rho_d \alpha_d \boldsymbol{u}_d)}{\partial t} + \nabla \cdot (\rho_d \alpha_d \boldsymbol{u}_d \boldsymbol{u}_d) = -\nabla \alpha_d P_d + \nabla \cdot \left[\alpha_d \mu_d \left(\nabla \boldsymbol{u}_d + \nabla \boldsymbol{u}_d^T\right)\right], \tag{13}$$

$$\frac{\partial(\rho_c \alpha_c \boldsymbol{u}_c)}{\partial t} + \nabla \cdot (\rho_c \alpha_c \boldsymbol{u}_c \boldsymbol{u}_c) = -\nabla \alpha_c P_c + \nabla \cdot \left[\alpha_c \mu_c \left(\nabla \boldsymbol{u}_c + \nabla \boldsymbol{u}_c^T\right)\right], \tag{14}$$

where P_d and P_c are the dispersed and continuous phase pressures. The above equation closely resembles the target E-E equations apart from the pressure term. Here, the pressures in each phase are independent, and their gradient terms dependent on the local variation in volume fraction.

A similar issue was also identified in the FV approach [39] which was solved by deriving and adding a correction term equal to $P\nabla\alpha_d$. Wang *et al.* [29] also introduced such a correction term in an LB context, while redefining α as the mass fraction to redefine phase pressures as a form of partial pressure. This approach recovered an approximation of the E-E equations. Zhang *et al.* [30] did something similar when simulating the volume-averaged Navier-Stokes equations in LB, but without accounting for the phase-specific pressures. However, this line of approach when using LB has been shown to be inaccurate in the presence of a volume fraction gradient and leads to instability [28,31]. Höcker *et al.* [31] therefore pursued a different path by modifying the LB streaming step to account for local differences in volume fraction. This indirectly generated the same correction term. While this approach does not suffer from discretization errors, our tests found it to be unstable for more dynamic flow conditions. In addition, these approaches only consider the contributions of the primary fluid phase to the pressure.

Another approach to the TF equations in LB was proposed by Song *et al.* [40] using a different definition of the zeroth moment in LB (based on total density instead of phase density) and a correction term similar to Zhang *et al.* [30]. A similar result was attained by Song *et al.* who inserted additional mass and momentum source terms into the nonconservative formulation of the Navier-Stokes equations. Blais *et al.* [28] also introduced a new collision term and a correction term that achieves similar results. However, both of these approaches have been applied to porous media flows only where the volume fraction is not as closely coupled via two separate Navier-Stokes equations.

Most of the solutions presented above add to each momentum equation a correction term that depends on the pressure calculated in all other phases. This leads to a set of highly coupled equations that tend to be susceptible to oscillations in the solution. In our tests, this leads to stability issues when modeling complex and chaotic systems such as turbulence. To overcome this challenge, we propose two approaches to recover the E-E equations in LB.

C. Approach 1: Poisson-based method

This approach uses a pressure-free variant of the LB method, along with a pressure Poisson equation and a volume fraction advection equation.

1. Pressure-free lattice Boltzmann method

The pressure-free (well-balanced) LB was proposed by Guo *et al.* [32] for simulations of thermodynamically accurate multiphase flows. He removed the pressure term in LB by modifying the equilibrium distribution function. Using this approach for the dispersed phase equation, we get

$$f_{i,d}(\mathbf{x}+\mathbf{c}_i\Delta t, t+\Delta t) - f_{i,d}(\mathbf{x},t) = \frac{\Delta t}{\tau}\left(f_{i,d}(\mathbf{x},t) - f^{\mathrm{eq}}_{i,d}(\mathbf{x},t)\right) + \Delta t\left(1-\frac{1}{2\tau}\right)F_{i,d}, \tag{15}$$

$$f^{\mathrm{eq}}_{i,d} = \begin{cases} \rho_d\alpha_d - (1-w_0)\rho_0 + w_0\rho_d\alpha_d s_0(\boldsymbol{u}_d), & i=0, \\ w_i(\rho_0 + \rho_d\alpha_d s_i(\boldsymbol{u}_d)), & i\neq 0, \end{cases} \tag{16}$$

$$s_i(\boldsymbol{u}_d) = \frac{\boldsymbol{c}_i\cdot\boldsymbol{u}_d}{c_s^2} + \frac{(\boldsymbol{c}_i\cdot\boldsymbol{u}_d)^2}{2c_s^4} - \frac{\boldsymbol{u}_d\cdot\boldsymbol{u}_d}{2c_s^2}, \tag{17}$$

$$F_{i,d} = w_i\left[\frac{\boldsymbol{c}_i\cdot\boldsymbol{F}_d}{c_s^2} + \frac{\boldsymbol{u}_d\left(\boldsymbol{F}_d + c_s^2\nabla(\rho_d\alpha_d)\right):\left(\boldsymbol{c}_i\boldsymbol{c}_i - c_s^2\mathbf{I}\right)}{c_s^4} + \frac{1}{2}\left(\frac{\boldsymbol{c}_i^2}{c_s^2} - D\right)(\boldsymbol{u}_d\cdot\nabla(\rho_d\alpha_d))\right], \tag{18}$$

where D is the number of spatial dimensions, $\mathbf{I}$ is the identity matrix, and ρ_0 is a numerical constant. In our testing, ρ_0 is set to zero following the original work by Guo *et al.* [32]. However, a nonzero value may be required to ensure positive f values when using inlet or outlet boundary conditions. Guo [32] includes a chemical potential based external force to replace the pressure term to complete the thermodynamically accurate well-balanced LB. Excluding this term, the resultant macroscopic model equations can be written as

$$\frac{\partial(\rho_d\alpha_d\boldsymbol{u}_d)}{\partial t} + \nabla\cdot(\rho_d\alpha_d\boldsymbol{u}_d\boldsymbol{u}_d) = \nabla\cdot\left[\alpha_d\mu_d\left(\nabla\boldsymbol{u}_d + (\nabla\boldsymbol{u})_d^T\right) + (\nabla\cdot\boldsymbol{u}_d)I\right] + \boldsymbol{F}_d, \tag{19}$$

where $\boldsymbol{F}_d$ constitutes all external forces—to which, see further on, a pressure term will be added. The new viscous stress term deviates slightly from the standard definition (by an error term proportional to the divergence) which will be discussed in the following section. The derivation of the above macroscopic equations can be found in the original work by Guo [32]. This variant of the standard LB equilibrium naturally removes the pressure term without an additional correction term. The method also preserves the lower moments of the distribution function, leading to an unchanged equation for density and momentum [see Eq. (5)]. The same approach can be used to derive the pressure-free LB equations for the continuous phase.

With this pressure-free LB scheme, the final E-E equations can be achieved by explicitly adding the correct pressure term as an external force. The added term should ensure a divergence-free mixture velocity field. Two methods to achieve this were identified in this study. The first approach utilizes a pressure Poisson equation to calculate the local pressure, while the second approach takes a mixture equation approach to noniteratively calculate the pressure within the LB framework. Below, we will visit each of these methods in detail and identify their strengths and weaknesses.

2. Pressure Poisson equation

Most finite volume solvers utilize the pressure Poisson equation to ensure a divergence-free velocity field. This equation can be solved by either finite volume [33] or LB methods [34]. While the LB approach can be faster, it is known to be inaccurate when the relaxation time τ [see Eq. (15)] departs from unity. Therefore, we utilize the finite volume approach as

$$\frac{1}{\Delta t}\nabla \cdot \boldsymbol{u}_m^* = \nabla \cdot \frac{\nabla P}{\rho_m}, \tag{20}$$

where $\boldsymbol{u}_m^*$ is the mixture velocity ($*$ representing pre-pressure-correction quantities) defined as $\boldsymbol{u}_m^* = \sum \alpha_k \boldsymbol{u}_k$. The solution procedure is similar to the work by Shu *et al.* [34]. Since this procedure minimizes the divergence of the velocity field, the error term in the viscous stress tensor (see Sec. II C 1) can be controlled by using appropriate residual thresholds. In this study, the simple Gauss-Seidel method is used to solve the Poisson equation.

3. Volume fraction advection equation

While the above modified LB method can reproduce the continuity equations, and thus the component transport, this method was found to lead to instability in the solution. Therefore, we use a finite volume approach to separately solve the advection equation [see Eq. (1)] for the dispersed phase, assuming that each phase is incompressible and obey their own continuity equation (nonconservative form). The resulting equation can be written as

$$\frac{\partial \alpha_d^{\mathrm{FV}}}{\partial t} + \boldsymbol{u}_d \cdot \nabla \alpha_d^{\mathrm{FV}} = 0. \tag{21}$$

This equation is explicitly solved in this study by using the forward Euler method for time discretization and first-order upwind scheme for the convection terms. The volume fraction from the above equation is coupled with the pressure-free LB equation. In practice, this requires the modification of the zeroth order moment in LB to the local component mass dictated by the advection equation. We thus modify the zeroth order as

$$\sum_i f_{i,d}^{\mathrm{eq}} = \rho_d \alpha_d^{\mathrm{FV}}. \tag{22}$$

As a result, the macroscopic momentum equation for the dispersed phase [see Eq. (19)] is modified to

$$\frac{\partial\left(\rho_d \alpha_d^{\mathrm{FV}} \boldsymbol{u}_d\right)}{\partial t} + \nabla \cdot \left(\rho_d \alpha_d^{\mathrm{FV}} \boldsymbol{u}_d \boldsymbol{u}_d\right) = \nabla \cdot \left[\alpha_d \mu_d \left(\nabla \boldsymbol{u}_d + \nabla \boldsymbol{u}_d^T\right) + (\nabla \cdot \boldsymbol{u}_d) I\right] + \boldsymbol{F}_d', \tag{23}$$

$$\boldsymbol{F}_d' = \alpha_d^{\mathrm{FV}} \nabla P + \boldsymbol{F}_D, \tag{24}$$

where $\boldsymbol{F}_D$ is the drag force. This modification enables us to account for the variation in component mass in the convective and transient terms. A similar approach can be used to obtain the equations for the continuous phase.

4. Summary

Combining the various components described above, the Poisson-based approach proposed here can be summarized to entail two pressure-free LB equations for the component momentum balances, a pressure Poisson equation and a FV advection equation for the dispersed phase volume fraction. This combination of equations results in the full Euler-Euler (or two-fluid) equations, though at the expense of discarding the noniterative nature of LB, which significantly affects the computational cost. While various optimized techniques can be used to accelerate the solution of the Poisson equation, an increase in computational cost compared to the native LB models is inevitable.

D. Approach 2: Mixture-based model

Overcoming the computational disadvantage of the Poisson-based model by avoiding the iterative Poisson equation requires the calculation of pressure to be performed within the LB equation. Coupling a pressure-free LB for the dispersed phase with a standard LB for the continuous phase would result in a pressure field that looks solely at the divergence of the continuous phase velocity field. Instead, we propose the coupling of a two-phase mixture equation with a modified incompressible LB equation for the dispersed phase. The following section describes our approach to the mixture-based approach and the coupling needed to recover the correct pressure and E-E equations.

1. Momentum equation for the two-phase mixture

The mixture equation [34,35] solves the conservation equations for the mixture of various phases, as opposed to each individual phase. This equation can be derived by a summation of all the phase momentum equations and can be written as

$$\frac{\partial}{\partial t}(\rho_m \boldsymbol{u}_m) + \nabla \cdot (\rho_m \boldsymbol{u}_m \boldsymbol{u}_m) = -\nabla P + \nabla \cdot \left[\mu_m \left(\nabla \boldsymbol{u}_m + \nabla \boldsymbol{u}_m^T\right)\right] + \boldsymbol{F}_m^C, \tag{25}$$

where the subscript m indicates mixture properties, and $\mathbf{F}_m^C$ is a correction term associated with the mixture equation and given as $\mathbf{F}_m^C = \nabla \cdot \tau_{Dm}$ with $\tau_{Dm} = -\sum_{k=1}^{n} \alpha_k \rho_k \mathbf{u}_{mk} \mathbf{u}_{mk}$ and $\mathbf{u}_{mk} = \mathbf{u}_k - \mathbf{u}_m$ being the phase velocity relative to the mixture (also called the diffusion velocity). The full derivation of the mixture model follows the original work by Manninen *et al.* [35] and can be found in Appendix A. The formulation of the mixture viscous dissipation term requires the use of a single velocity gradient approximation (see Appendix A) which is valid when both phases have similar velocity gradients.

The mixture equation involves the correct pressure term (without the volume fraction multiplier). Direct application of the LB model to this equation however requires a constant mixture density (nearly incompressible), which is often not true. Hence, we modify the mixture momentum equation into the "phase intensive" (PI) form [41–43]. This is done by first converting the momentum equations to their nonconservative forms Hence, we can further rescale the mixture equation by the phase density to derive the PI formulation of the mixture equation. The new PI mixture equation becomes

$$\frac{\partial}{\partial t}(\boldsymbol{u}_m) + \nabla \cdot (\boldsymbol{u}_m \boldsymbol{u}_m) = \frac{1}{\rho_m}\left[-\nabla P + \nabla \cdot \left[\mu_m \left(\nabla \boldsymbol{u}_m + \nabla \boldsymbol{u}_m^T\right)\right] + \boldsymbol{F}_m^C + \boldsymbol{F}_{\mathrm{PI}}^C\right], \tag{26}$$

$$\boldsymbol{F}_{\mathrm{PI}}^C = \nabla \rho_m \cdot \left(\nabla \cdot \left[\mu_m \left(\nabla \boldsymbol{u}_m + \nabla \boldsymbol{u}_m^T\right)\right]\right), \tag{27}$$

where $\boldsymbol{F}_{\mathrm{PI}}^C$ is the correction term associated with the phase intensive formulation. This equation can be rearranged as

$$\frac{\partial}{\partial t}(\boldsymbol{u}_m) + \nabla \cdot (\boldsymbol{u}_m \boldsymbol{u}_m) = -\nabla P + \nabla \cdot \left[\mu_m \left(\nabla \boldsymbol{u}_m + \nabla \boldsymbol{u}_m^T\right)\right] + \frac{\boldsymbol{F}_m}{\rho_m}, \tag{28}$$

$$\boldsymbol{F}_m = (\rho_m - 1)\nabla P + \boldsymbol{F}_m^C + \boldsymbol{F}_{\mathrm{PI}}^C, \tag{29}$$

where $\boldsymbol{F}_m$ contains the correction terms. The full derivation of the above equations can be found in Appendix B.

The PI approach is often used in E-E models to improve stability in the presence of large density ratios [41,42,44,45]. The new governing equation now accumulates the mass dependent terms into a separate correction term and takes a form similar to the incompressible NS equations with a modified pressure term and additional correction terms to account for the local variations in density.

2. Incompressible lattice Boltzmann method

Standard LB couples the density and pressures together, making it valid only when ρ remains nearly constant. This makes the standard LB a nearly incompressible method which is a valid approach for single-phase flows. However, application of the standard LB method to solve Eq. (26) would lead to the convective and transient terms being multiplied by a pseudodensity proportional to the pressure, which is undesirable. Modifying the LB equations to make them incompressible can remove the density from the equation, making it easier to work with. Various approaches have been established in literature to achieve this [33,46–49]. For simplicity, here we follow the approach proposed by He *et al.* [46]. This method modifies the equilibrium distribution function as

$$f_i^{\mathrm{eq}} = w_i\left[\rho + \rho_1\left(\frac{\boldsymbol{c}_i\cdot\boldsymbol{u}}{c_s^2} + \frac{(\boldsymbol{c}_i\cdot\boldsymbol{u})^2}{2c_s^4} - \frac{\boldsymbol{u}\cdot\boldsymbol{u}}{2c_s^2}\right)\right], \tag{30}$$

which modifies the moments as

$$\textstyle\sum_i f_i^{\mathrm{eq}} = \rho, \quad \sum_i \boldsymbol{c}_i f_i^{\mathrm{eq}} = \rho_1\boldsymbol{u}, \tag{31}$$

where ρ_1 is a constant, often taken to be unity by convention. The pressure is then given by $P = c_s^2\rho$. A Chapman-Enskog expansion can be used to show that these modifications lead to the following incompressible Navier-Stokes equation:

$$\nabla\cdot\boldsymbol{u} = 0, \tag{32}$$

$$\frac{\partial(\boldsymbol{u})}{\partial t} + \nabla\cdot(\boldsymbol{u}\boldsymbol{u}) = -\frac{\nabla P}{\rho_1} + \nabla\cdot[\nu(\nabla\boldsymbol{u} + \nabla\boldsymbol{u}^T)] + \frac{\boldsymbol{F}}{\rho_0}, \tag{33}$$

where $\boldsymbol{F}$ contains all external forces.

Recognizing the similarity between the above model and the mixture equations [see Eq. (28)], the incompressible LB can be written for the mixture equation as

$$\nabla\cdot\boldsymbol{u}_m = 0, \tag{34}$$

$$\frac{\partial(\boldsymbol{u}_m)}{\partial t} + \nabla\cdot(\boldsymbol{u}_m\boldsymbol{u}_m) = -\frac{\nabla P}{\rho_1} + \nabla\cdot\left[\mu_m\left(\nabla\boldsymbol{u}_m + \nabla\boldsymbol{u}_m^T\right)\right] + \frac{\boldsymbol{F}_m}{\rho_0\rho_m}, \tag{35}$$

where μ_m is the mixture dynamic viscosity, which may be defined as the mass average between the components, or using a separate model. In this study, the mass-averaged value is used unless otherwise mentioned. The above method hence obtains an LB model for the mixture equation that produces the pressure term within the LB framework. However, since the local density has been decoupled from the LB distribution functions, the pressure generated assumes an incompressible mixture phase. This assumption holds well in the absence of sharp interfaces and high gradients in density, as we will show in the following sections.

3. Momentum equation for the dispersed phase

To complete the mixture model, a closure model is required for the diffusion velocity $\boldsymbol{u}_{mk}$. The simplest approach is to assume a constant value (assuming local equilibria) [34,50]. A simplified balance equation can also be used to solve for the relative velocity [35]. Instead, here we introduce another Navier-Stokes equation to simulate the dispersed phase akin to the complete E-E model.

Since the pressure forces would have to be added explicitly from the mixture equation, a pressure-free LB equation could be used for the dispersed phase. However, this would require additional correction terms that can be computationally expensive. Instead, we can modify the incompressible LB equation to be pressure-free by enforcing a constant zeroth-order moment, i.e., $\sum_i f_i^{\mathrm{eq}} = C$.

Setting the constant to unity, the new equilibrium distribution function becomes

$$f_{i,d}^{\text{eq}} = w_i\left[1 + \frac{\boldsymbol{c}_i \cdot \boldsymbol{u}_d}{c_s^2} + \frac{(\boldsymbol{c}_i \cdot \boldsymbol{u}_d)^2}{2c_s^4} - \frac{\boldsymbol{u}_d \cdot \boldsymbol{u}_d}{2c_s^2}\right], \tag{36}$$

$$\textstyle\sum_i f_i^{\text{eq}} = 1, \quad \sum_i \boldsymbol{c}_i f_i^{\text{eq}} = \boldsymbol{u}_d, \tag{37}$$

and the corresponding Navier-Stokes equation becomes

$$\frac{\partial(\boldsymbol{u}_d)}{\partial t} + \nabla \cdot (\boldsymbol{u}_d \boldsymbol{u}_d) = \nabla \cdot \left[\nu_d\left(\nabla \boldsymbol{u}_d + \nabla \boldsymbol{u}_d^T\right)\right]. \tag{38}$$

Using the Shan-Chen approach of forces in LB, the PI correction term ($\boldsymbol{F}_{\text{PI},d}^C = \sigma_{\alpha\beta,d} \cdot \nabla(\rho_d \alpha_d)$), pressure, and drag forces can be explicitly added to give the final Navier-Stokes equation as

$$\frac{\partial(\boldsymbol{u}_d)}{\partial t} + \nabla \cdot (\boldsymbol{u}_d \boldsymbol{u}_d) = \nabla \cdot \left[\nu_d\left(\nabla \boldsymbol{u}_d + \nabla \boldsymbol{u}_d^T\right)\right] + \frac{\boldsymbol{F}_d}{\rho_d \alpha_d}, \tag{39}$$

$$\boldsymbol{F}_d = -\alpha_d \nabla P + \boldsymbol{F}_{\text{PI},d}^C + \boldsymbol{F}_D, \tag{40}$$

where $\boldsymbol{F}_D$ is the drag force.

4. Summary

Similar to the Poisson-based model, an advection equation is used for the volume fraction. A phase intensive formulation is used for the pressure-free LB (for the dispersed phase). This forms the coupling between the volume fraction advection equation and the momentum equation for the dispersed phase. These result in the following set of Navier-Stokes equations:

$$\frac{\partial(\boldsymbol{u}_m)}{\partial t} + \nabla \cdot (\boldsymbol{u}_m \boldsymbol{u}_m) = -\frac{\nabla P}{\rho_0} + \nabla \cdot \sigma_{\alpha\beta,m} + \frac{\boldsymbol{F}_m}{\rho_0 \rho_m}, \tag{41}$$

$$\frac{\partial(\boldsymbol{u}_d)}{\partial t} + \nabla \cdot (\boldsymbol{u}_d \boldsymbol{u}_d) = \nabla \cdot \sigma_{\alpha\beta,d} + \frac{\boldsymbol{F}_d}{\rho_d \alpha_d}, \tag{42}$$

$$\boldsymbol{F}_m = (\rho_m - 1)\nabla P + \boldsymbol{F}_m^C + \boldsymbol{F}_{\text{PI}}^C, \tag{43}$$

$$\boldsymbol{F}_d = \alpha_d \nabla P + \boldsymbol{F}_{\text{PI},d}^C + \boldsymbol{F}_D, \tag{44}$$

$$\frac{\partial \alpha_k^{\text{FV}}}{\partial t} + \boldsymbol{u}_k \cdot \nabla \alpha_k^{\text{FV}} = 0, \tag{45}$$

where k represents the dispersed phase and $\boldsymbol{F}_D$ is the drag force. It should be noted that the error in the viscous term of the pressure-free LB is retained and cannot be explicitly controlled since residual thresholds cannot be specified.

E. Interphase momentum transfer

The external forces applied to each phase include internal interactions like drag, lift, virtual mass, turbulent dispersion, etc., and external forces such as gravity. In this study, only the drag force is included for interphase interactions. The drag force is defined here as

$$\boldsymbol{F}_D = \frac{18\alpha_d \alpha_c \mu_c f_D}{d_p^2}(\boldsymbol{u}_d - \boldsymbol{u}_c), \tag{46}$$

where d_p is the Sauter mean diameter, $\text{Re}_p = \rho_c d_p |\boldsymbol{u}_d - \boldsymbol{u}_c|/\mu_c$, subscript p denotes the dispersed phase, f_D is a function of the drag coefficient written as $f_D = \frac{\text{Re}_p}{24} C_D$ in which C_D is the drag coefficient defined as $C_D = \frac{24}{\text{Re}_p}(1 + 0.15\text{Re}_p^{0.687})$ based on the Schiller-Naumann model [51]. In practice, large drag forces can induce oscillations and subsequent divergence of the solution in LB.

In FV methods, reducing the time step size can solve this issue but that is not possible in LB. Using subtimesteps for the forcing can improve stability but significantly increases computational cost.

In this study, we reinterpret the forcing part of LB as a differential equation and emulate subtimesteps by exponentially decaying the velocity toward the equilibrium slip velocity. Using the Shan-Chen-style forcing [52], the velocity is updated as

$$\boldsymbol{u}_c^* = \boldsymbol{u}_c + \Delta t \frac{\boldsymbol{F}_c^{\text{ext}}}{2\rho_c} + \Delta t \frac{\boldsymbol{F}_D}{2\rho_c}, \tag{47}$$

where the forces acting on the continuous phase (subscript c) are decomposed into external forces $\boldsymbol{F}_c^{\text{ext}}$ and interphase forces. Here, only the drag force $\boldsymbol{F}_D$ is considered. This forcing can be split into two steps as

$$\boldsymbol{u}_c^+ = \boldsymbol{u}_c^0 + \Delta t \frac{\boldsymbol{F}_c^D}{2\rho_c}, \tag{48}$$

$$\boldsymbol{u}_c^* = \boldsymbol{u}_c^+ + \Delta t \frac{\boldsymbol{F}_c^{\text{ext}}}{2\rho_c}, \tag{49}$$

where $\boldsymbol{u}_c^0$ is the velocity value at the previous time step, and $\boldsymbol{u}_c^+$ is an intermediate value. Allowing for subtimesteps in the first step by letting Δt tend to 0, this equation can be rewritten as differential equations as

$$\frac{d\boldsymbol{u}_c}{dt} = \frac{\boldsymbol{F}_D}{2\rho_c}. \tag{50}$$

In essence, the drag force can now be implemented integrally first, followed by the standard implementation of all other external forces. Assuming a simple form of drag force as $\boldsymbol{F}_D = \lambda(\boldsymbol{u}_d - \boldsymbol{u}_c)$ where λ accumulates all the constants, the differential equation can be rewritten as

$$\frac{d\boldsymbol{u}_c}{dt} = \frac{\lambda(\boldsymbol{u}_d - \boldsymbol{u}_c)}{2\rho_c}. \tag{51}$$

Since the drag force does not affect the mixture momentum $\rho_m \boldsymbol{u}_m$, its definition can be used to eliminate the dispersed phase velocity from the above equation as

$$\frac{d\boldsymbol{u}_c}{dt} = \frac{\lambda}{2\rho_c}\left(\frac{\rho_m \boldsymbol{u}_m - \rho_c \boldsymbol{u}_c}{\rho_d} - \boldsymbol{u}_c\right) = \frac{\lambda \rho_m u_m}{2\rho_c \rho_d} - \frac{\lambda(\rho_c + \rho_d)}{2\rho_d \rho_c}\boldsymbol{u}_c. \tag{52}$$

Defining constants $\mathbf{A} = \frac{\lambda \rho_m \boldsymbol{u}_m}{2\rho_c \rho_d}$ and $B = \frac{\lambda(\rho_c+\rho_d)}{2\rho_d \rho_c}$, the equation can be rewritten and solved to give

$$\boldsymbol{u}_c^+ = \frac{\mathbf{A} - \left(\mathbf{A} - B\boldsymbol{u}_c^0\right)e^{-Bt}}{B}. \tag{53}$$

This intermediate velocity is then used in Eq. (49) with $\Delta t = 1$ (standard in LB). This formulation ensures an oscillation-free drag force. This principle is slightly adapted for each of the proposed methods, but the overall procedure remains the same.

III. VALIDATION

The two new models presented in Sec. II need to be validated against known solutions to prove their accuracy. In this section, we first validate the models for two test cases: a falling swarm of particles and a Rayleigh-Taylor instability. This varied choice in test cases is intended to demonstrate the flexibility and robustness of the proposed methods. The results presented here validate the models against existing literature data and compare the two models in terms of accuracy.

A. Falling cloud

This test case considers a cloud of particles, originally of a spherical shape, falling under the action of gravity. It illustrates how in this E-E (or two-fluid) approach, the particulate phase is conceived as a continuum—implying individual particles can't be discerned—while modeling the interactions of the particles in the swarm with the fluid. In practice, this involves representing the local dispersed phase distribution in any lattice cell with the fraction of the cell volume occupied by the dispersed phase (α_d). Another reason for choosing this case is the presence of sharp gradients in the volume fraction of particles, which is a good test of the stability of these approaches.

1. Case setup

This test case is conducted in a cuboidal domain with dimensions of $W \times W \times 2W$, where W is the size of the domain in the periodic x and y directions, with $2W$ being the height of the domain bounded by horizontal no-slip walls. W is taken to be 64 lattice units in this case. In physical units, $W = 0.1$ m. The simulation conditions match those used by Heidler *et al.* [53]. A spherical swarm of the dispersed particulate phase is initialized with a radius of 0.03 m at the center of the cross section and $3W/2$ lattice units from the bottom. For spherical particles, the volume fraction of the dispersed phase in any lattice cell within the cloud can be calculated as the ratio of volume occupied by the particles to the volume of the cell ($\alpha_d = \frac{n_p \pi d_p^3/6}{\Delta x^3}$, where n_p is the number of particles in a lattice cell, and Δx is the lattice cell side length). At high particle phase densities, the volume fraction may be limited by the packing density of the particles. In this study, the volume fraction within the swarm is chosen to be 0.11 to match the reference test case [53]. The edges of the cloud were smoothened to avoid any extreme gradients in the initialization. The density ratio between the solid and liquid phases is taken to be 1.5 and the kinematic viscosity of the continuous phase is taken as 10^{-4} m^2/s. Switching to LB units, the relaxation time is taken as 0.51627. The dynamic viscosity of the particulate phase is calculated using the Krieger-Dougherty model [54] which can be written as

$$\mu_d = \mu_c \left(1 - \frac{\alpha_d}{\alpha_p}\right)^{-2.5\alpha_p}, \tag{54}$$

where α_p is the maximum packing fraction, taken here as 0.62. The evolution of the swarm is qualitatively compared with Heidler *et al.* [53].

2. Results

Figure 1 shows the progress of the particle cloud falling under gravity for the two proposed models and the reference solution, with the columns (left to right) showing the progression with time. The contours represent a central 2D slice of the volume fraction distribution in the system. Heidler *et al.* compares the E-E approach (black line) with the E-L approach (red line). At time $t = 0.5$ s, both models show a deformation of the cloud from its initial spherical shape, in line with the behavior expected on the basis of the literature. Both models are almost indistinguishable at this stage, the mixture model showing a slightly higher artificial diffusion at the cloud interfaces. This can be observed as a slightly wider transition from the cloud to the surrounding fluid. The effect can be clearly seen when plotting the volume fraction along a horizontal line through one side of the cloud (see the red dashed line in the second image on the top row in Fig. 1), as seen in Fig. 2. This difference may be attributed to its simplified density-free pressure, which creates noticeable errors in the presence of sharp density gradients.

By $t = 0.83$ s and $t = 1.5$ s both models show the cloud adopting a similar "U" shape that compares well with the solution from the literature. Finally, at $t = 2.33$ s, the cloud takes a lobed shape, with the Poisson model exhibiting sharper gradients and more pronounced structures. Both models qualitatively match the literature, although our models exhibit longer lobes at the final instance shown. The differences in shape near the bottom wall can be attributed to a need for

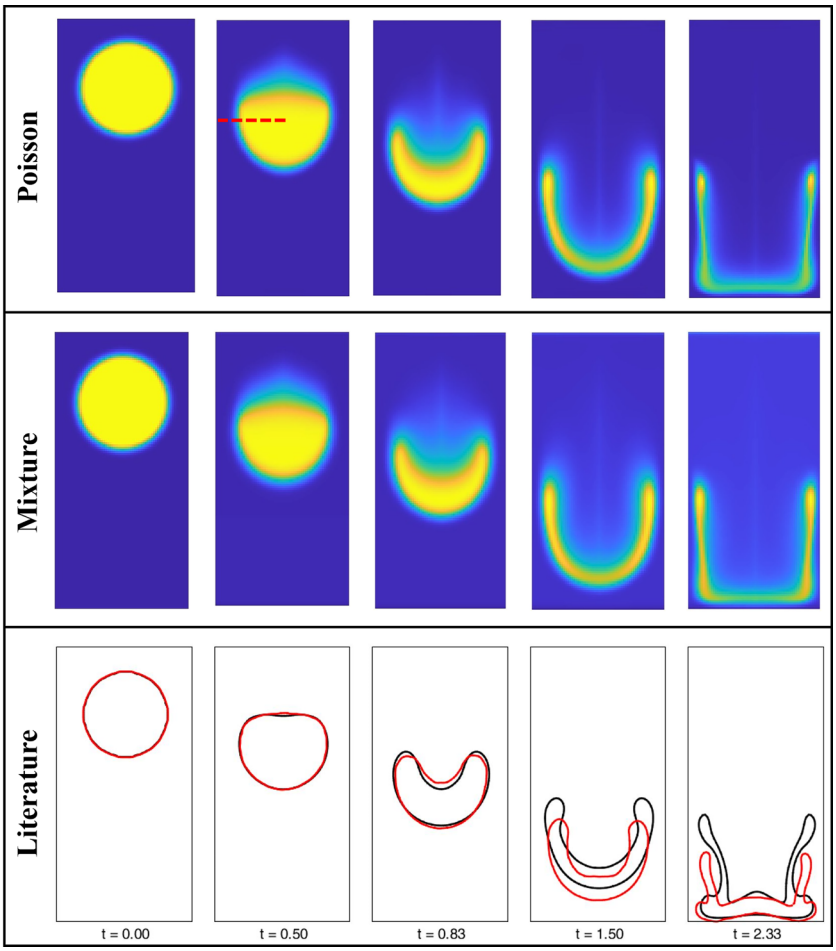


FIG. 1. Time evolution of the volume fraction in a falling cloud of particles, originally of a spherical shape, using the proposed E-E models (first and second rows). Yellow corresponds to $\alpha_d = 0.11$ and blue corresponds to $\alpha_d \approx 0$. The red dashed line in the second image (row 1 column 2) depicts the line used to plot the volume fraction in Fig. 2. The results are qualitatively compared with literature [53] (third row) with the red and black lines representing solutions from a E-L and E-E solver, respectively. Time is given in seconds.

higher-order schemes near the wall. The higher diffusion in the mixture model can also be observed in the figures as a slightly elevated ambient volume fraction.

B. Rayleigh-Taylor instability

This standard test case demonstrates the evolution of gravity-induced instability at a perturbed interface in a multiphase system. First introduced by Rayleigh [55], and subsequently applied by Taylor [56], this instability is very commonly observed in numerous fields [57–59]. Due to its wide range of applications, it has been extensively studied [60–62]. Therefore, Rayleigh-Taylor instability can be used as a good validation case to test the accuracy of our models.

1. Case setup

The simulation domain is taken to be cuboidal in shape and is initialized with the top half containing the dispersed phase and the bottom half purely the continuous one. The interface between

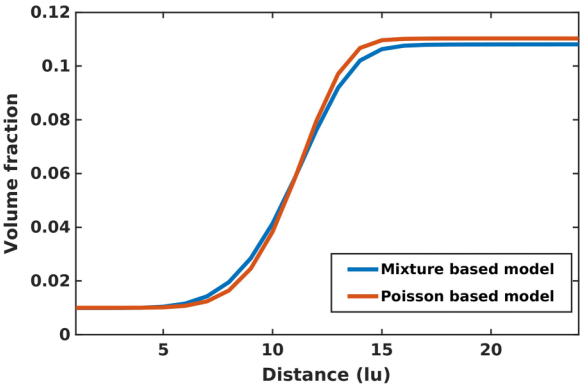


FIG. 2. Plot of the volume fraction along a horizontal line from the domain boundary to the center of the cloud at $t = 0.50$ s. The line used is depicted in the second image on the top row (row 1 column 2) in Fig. 1.

the phases is initialized with a square-mode perturbation as

$$h(x, y) = 0.05W[\cos(kx) + \cos(ky)], \tag{55}$$

where W is the width of the domain, and $k = 2\pi/W$ is the wave number. The initial interface is slightly smoothed using a hyperbolic tan function to improve numerical stability. The vertical dimension is taken to be $12W$. The top and bottom boundaries are set to no-slip walls and all other boundaries are periodic. The flow is described by the Reynolds number (Re) and the Atwood number (At) [63] defined as

$$\mathrm{Re} = \frac{W\sqrt{gW}}{\nu}, \tag{56}$$

$$\mathrm{At} = \frac{\rho_l - \rho_g}{\rho_l + \rho_g}. \tag{57}$$

In this study, the Reynolds number and Atwood number are taken to be 10 and 0.15, respectively, to match with the literature of choice. The domains are created with $W = 32$ lu and $W = 48$ lu, both significantly lower than the $W = 100$ lu used in the literature. For each value of W, the relaxation time τ is chosen to obtain the required Reynolds number. The acceleration due to gravity g is taken to be 3.4×10^{-6} lu ts^{-2} in most cases unless the required τ value rises above unity, in which case g is reduced. Along with the wave number k, this results in a (varying) timescale $(gk)^{-0.5}$ and a (varying) velocity scale $\sqrt{gW}$. The gravitational force is implemented in both models as a constant downward force, which automatically generates the static pressure forces.

2. Results

Figure 3 gives the volume fraction contours for the time evolution of the Rayleigh-Taylor instability for the Liang *et al.* [60] conditions. These reference solutions were obtained using a new multiple relaxation time-based LB method with a new multiphase model. This can be compared with the contours for our proposed Poisson-based and mixture-based models. Both models proposed by us show qualitative behavior similar to the solution reported by Liang *et al.*, accurately capturing the initial perturbation growth and the finger elongation. Our interfaces are noticeably thicker, partly due to our initial condition and partly due to the use by Liang *et al.* of a multiphase interface model. As indicated above, the interface is more diffuse in our mixture-based model due to the error in the pressure correction in the presence of sharp density gradients.

Figure 4 shows the evolution of the amplitude of the instability with time for the two models and compared to the literature. The effect of the excessive diffusion at the interface in the

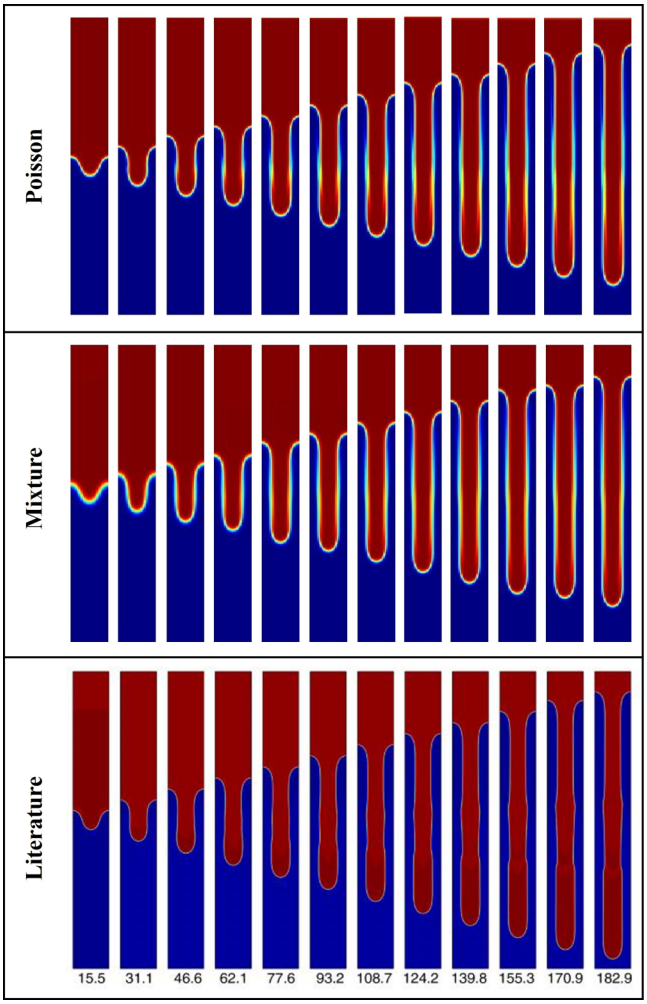


FIG. 3. Density contours showing the evolution of the volume fraction with time for Re = 10. The results from the Poisson-based and mixture-based models are compared with literature [60]. The time is normalized by the characteristic modified timescale $\mathrm{At}^{-0.5}(gk)^{-0.5}$ where At stands for the Atwood number and k denotes the wave number.

mixture-based model can be observed as a slight offset in the depth curve. This offset propagates to later stages consistently. Both models can be seen to converge toward the literature solution as the resolution is increased. The deviation is seen to increase with time. This can be attributed to the increasing surface area of the interface, leading to an increasing role for the pressure correction error. Increasing the resolution may minimize this error by decreasing the local gradients in the density. Taking into account the considerable difference in spatial resolution, these results can be concluded to be satisfactory in validating the proposed models for such test cases.

IV. LARGE EDDY SIMULATION OF HOMOGENEOUS ISOTROPIC TURBULENCE

The above test cases showcase the capability of the proposed models to simulate multiphase gravitational flows at lower Reynolds numbers. However, most industrial applications to E-E models involve varying degrees of turbulence. Therefore, a practically usable E-E model should be accurate and stable enough to simulate complex turbulent flows. In this section, we

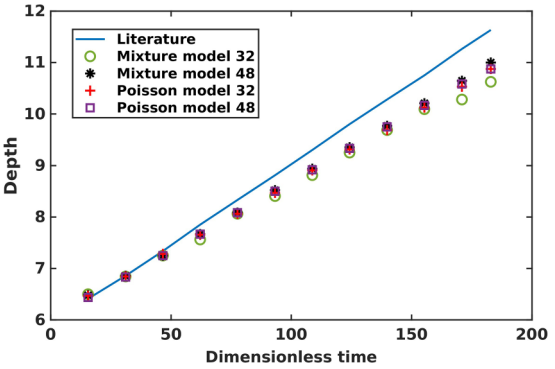


FIG. 4. Evolution of the normalized bubble amplitude with time for both Poisson-based and mixture-based models. Both models are presented here at two resolutions: $W = 32$ lu and $W = 48$ lu. The results are compared with literature, which uses a fully resolved model with $W = 100$ lu. The time is normalized by the characteristic time $\mathrm{At}^{-0.5}(gk)^{-0.5}$.

demonstrate this capability by modeling the creation of an emulsion in homogeneous isotropic turbulence (HIT).

A. Large eddy simulation

Large eddy simulations resolve most larger (and anisotropic) scales of turbulent flows while using SGS models to approximate the smaller (and isotropic) scales. By using the Boussinesq approximation, the effects of the SGS turbulence are modeled through an additional turbulence viscosity. The earliest and simplest SGS model was the static Smagorinsky model introduced by Smagorinsky in 1963 [64]. Based on this model, the kinematic viscosity is replaced by the effective viscosity ($\nu_{\text{eff}} = \nu + \nu_t$), where the turbulence viscosity (ν_t) can be written as

$$\nu_t = (C_s\Delta)^2|S|, \tag{58}$$

$$|S| = \sqrt{\frac{1}{2}\left(\frac{\partial u_i}{\partial x_j} + \frac{\partial u_j}{\partial x_i}\right)^2}, \tag{59}$$

where C_s is the Smagorinsky constant, Δ is the filter size, and $|S|$ is the characteristic strain rate.

Various values for C_s have been suggested over the years using varying approaches ranging from 0.065 to 0.23 [65–69]. For relatively well-resolved meshes, a popular analytically derived value is $C_s \approx 0.17$. However, assuming a constant value for C_s is known to be too simple. Zachariah *et al.* [70] observed C_s to vary extensively with the local strain rate. The dynamic Smagorinsky model [71–73] locally calculates C_s using additional filters and has been known to be more accurate than the static Smagorinsky model. Over the years, various advanced models have been developed to better represent the SGS turbulence [74,75]. Despite this development, the static Smagorinsky model is still widely used in the industry due to its simplicity and sufficient accuracy. Thus, to demonstrate our model's stability, we choose to use the static Smagorinsky model.

The static Smagorinsky model was first implemented in LBM by Hou *et al.* [76]. While the strain rate tensor can be calculated using a finite difference approach, LB offers an alternative approach which enables the local calculation of the strain rate tensor. By this approach, the local strain rate can be calculated as

$$S_{ij} = -\frac{T_{ij}}{2\rho c_s^2 \delta_t \tau^{\text{eff}}}, \tag{60}$$

where T_{ij} is the stress tensor which can be calculated locally using the nonequilibrium distribution function f^{neq} as

$$T_{ij} = \sum_{\alpha} e_{i,\alpha} e_{j,\alpha} f_{\alpha}^{\text{neq}}, \tag{61}$$

$$f_{\alpha}^{\text{neq}} = f_{\alpha} - f_{\alpha}^{\text{eq}}. \tag{62}$$

Using this definition, the local values of the turbulent viscosity can be calculated (see Yu *et al.* [77]) as

$$\nu_t = (C_S \Delta)^2 |S| = \frac{1}{6}\left(1 + \sqrt{\tau^2 + \frac{18(C_S\Delta)^2 T}{\rho}} - \tau\right), \tag{63}$$

where $T = \sqrt{2T_{ij}T_{ij}}$. This model is used in both liquid phases to obtain the turbulence viscosity, to get the effective viscosity as

$$\nu^{\text{eff}} = \nu + \nu_t. \tag{64}$$

1. Case setup

HIT is an idealized test case where turbulence is induced in an infinite domain with the help of a carefully formulated force that mimics the effects of the large scales of turbulent flow. Here, we apply the HIT force to a periodic box with two immiscible phases in it, leading to the emulsification of the mixture. The turbulent forcing method used by Mukherjee *et al.* [78] is employed here, with the forcing prescribed as

$$F_{x,\alpha} = \sum_{k=k_a}^{k_b} \frac{\rho_\alpha}{\rho} A(k)[\sin(ky + \phi_y(k)) + \sin(kz + \phi_z(k))],$$

$$F_{y,\alpha} = \sum_{k=k_a}^{k_b} \frac{\rho_\alpha}{\rho} A(k)[\sin(kx + \phi_x(k)) + \sin(kz + \phi_z(k))],$$

$$F_{\alpha} = \sum_{k=k_a}^{k_b} \frac{\rho_\alpha}{\rho} A(k)[\sin(kx + \phi_x(k)) + \sin(ky + \phi_y(k))], \tag{65}$$

where k is the wave number given by $k = 2\pi/\Phi$, ρ is the total density. k_a and k_b are the lower and higher limit for the wave numbers where the forcing is applied. The wave number can be written as multiples of the minimum wave number $k_{\min} = 2 \times \pi/n_x$ as $k = l \times k_{\min}$, where l is a constant. The forcing is applied in wave numbers ranging from $k_a = 1 \times k_{\min}$ to $k_b = 8 \times k_{\min}$ corresponding to $l_a = 1$ to $l_b = 8$.

All LESs in this section are performed using a cubical domain with length $n_x = 64$. The domain is initialized with zero velocity and uniform total density. The spherical swarm of the dispersed phase is initialized with a volume fraction of 0.5. Both phases are set to have equal density ($\rho_1 = \rho_2 = 4.0$ lu) and equal relaxation times ($\tau_1 = \tau_2 = 0.50088$). The choice of relaxation time is made to ensure equal time steps between LES and DNS simulations for easy comparison.

The models proposed in this study will be compared with exact solutions from DNSs. These are performed using the Shan-Chen multiphase method in LB with the two phases having equal phase densities and viscosities. The domain is taken to be cubical with a side length of 256 lattice units. The conditions match the P2 test case in the work by Mukherjee *et al.* [78]. This gives a characteristic timescale of 474 lattice time units, which is used to normalize time in the following results shown. The domain is initialized with a sphere of the dispersed phase in the center that occupies about 6% of the total volume. The high and low densities at equilibrium are $\rho_h = 4$ mass units and $\rho_l = 0.77$ mass units.

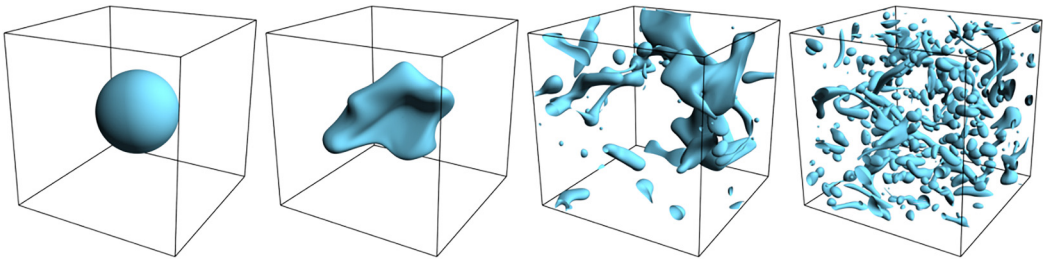


FIG. 5. Evolution of the emulsion with time from Mukherjee *et al.* [78]. Results from DNSs with the Shan-Chen multiphase LB method. Time instances shown here are $t/t_k \approx 0, 10, 40, 100$ [where $t_k = (\nu/\epsilon)^{0.5}$ is the Kolmogorov timescale].

2. Results

Figures 5 and 6 show the evolution of the initial droplet with normalized time for the DNS of Mukherjee *et al.* [78] alongside our reference DNSs. The iso-surfaces plotted define the interface at locations where $\rho = 0.5(\rho_h + \rho_l)$. The structures observed match well the results presented by Mukherjee *et al.* indicative of an accurate reference solution. The emulsification mechanism is seen to follow the same elongation and breakage mechanism observed in the literature [78]. The figures show the initial emulsification during 52 Kolmogorov timescales, but at least twice that time is required to reach a statistically steady state. At that stage, a statistical equilibrium is reached between the rates of coalescence and breakage of droplets.

Figure 7 shows the evolution of a similar emulsion when using the Poisson-based E-E model. The images from the mixture model have been omitted because hardly any noticeable difference is observed. The spherical geometry is preserved from the DNS with the volume fraction inside and outside the droplet set to 0.99 and 0.01, respectively. Since E-E models do not contain a well-defined interface, contour plots on a central slice of the domain are used to show the time evolution of the dispersed phase.

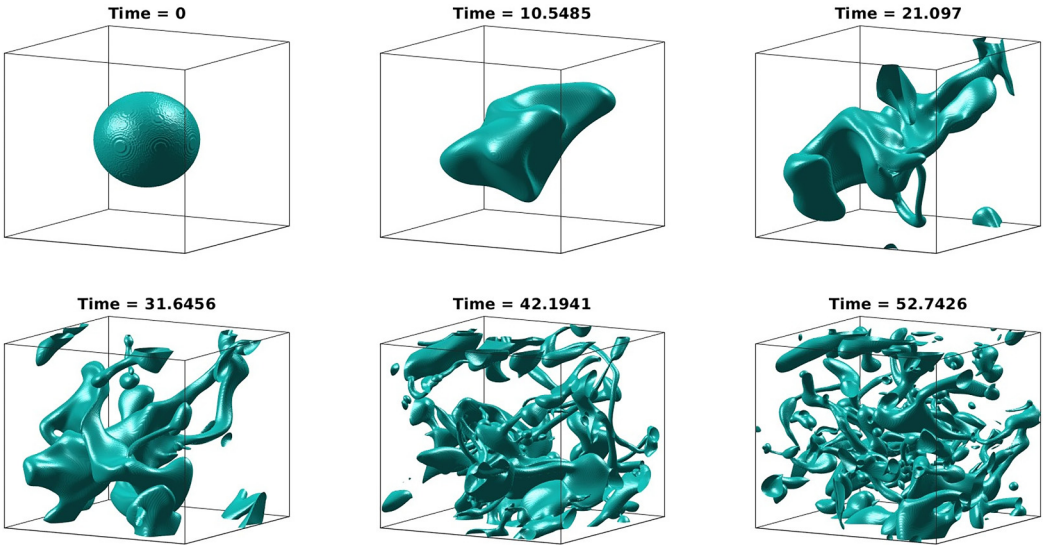


FIG. 6. Evolution of the emulsion with time for a full-scale DNS. The time is normalized by the Kolmogorov timescale $t_k(\epsilon/\nu)^{-0.5}$.

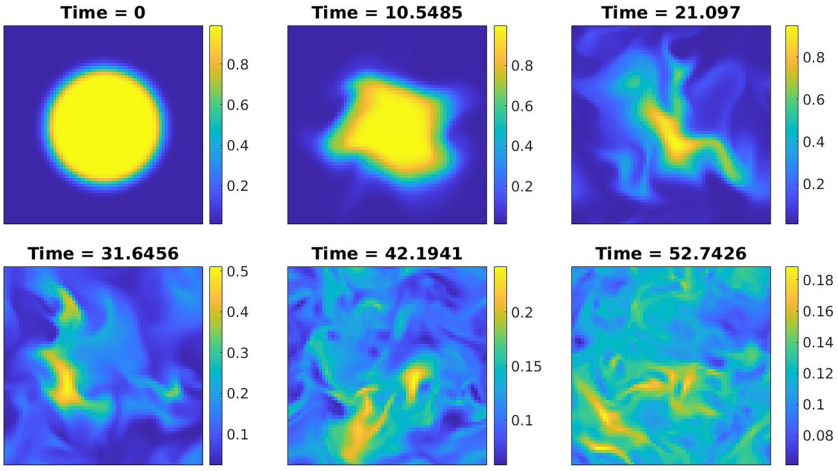


FIG. 7. Evolution of the emulsion with time for E-E model (Poisson approach) with the Smagorinsky SGS model. The time is normalized by the Kolmogorov timescale $t_k(\epsilon/\nu)^{-0.5}$.

Comparing the initial deformation (the first 10 Kolmogorov timescales), familiar structures are observed, implying that the turbulent forcing primarily directs the deformation in both DNS and E-E LES. As the droplet deforms in the DNS (Fig. 6), surface tension begins to dominate, leading to the creation of smaller (and more stable) droplets. The lack of surface tension in the E-E model means it does not account for this mechanism. The drop interface diffuses out with turbulent flow field without the surface tension to hold the drop together. At about 21 Kolmogorov time steps, the drop-like structures start to be dissipated and the density contour begins to resemble a turbulent flow field. Shifting now to a quantitative perspective, Fig. 8 compares the averaged turbulence spectrum from the DNS of an emulsion (normalized with the area under the curve) to high-resolution E-E simulations using both mixture-based and Poisson-based approaches. A single-phase DNS spectrum is also shown for comparison, although it has been scaled to overlap with the emulsion spectrum for better comparison. When the DNS emulsion spectrum is compared with the DNS single-phase

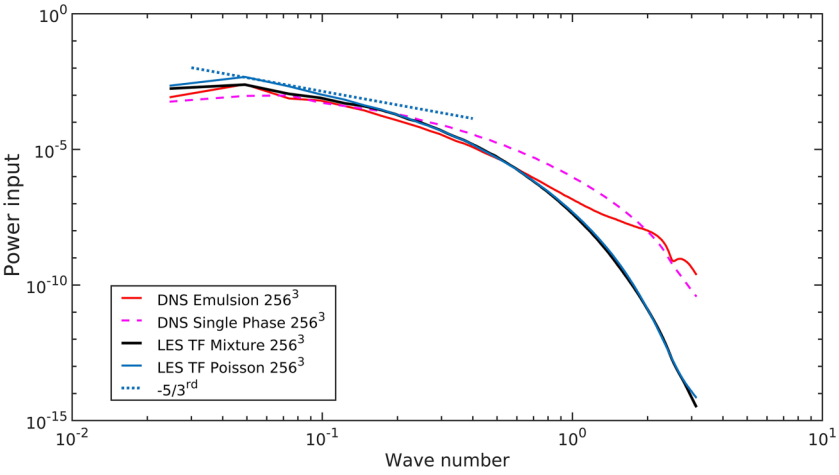


FIG. 8. Time-averaged normalized turbulence spectra from DNS simulations with and without dispersed phase compared with our high-resolution (256^3) E-E mixture-based and Poisson-based LES results. Both E-E models agree well with the emulsion DNS at large and intermediate scales.

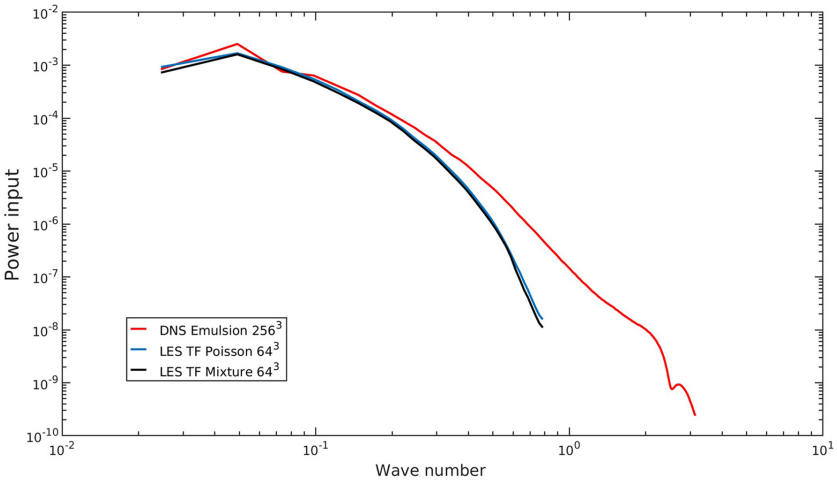


FIG. 9. Time-averaged turbulence spectra from DNS of emulsion compared with our coarser (64^3) E-E LESs based on both the mixture-based and Poisson-based approaches. Both LESs match well with the emulsion DNS at large and intermediate scales but deviate strongly at the smallest scales.

spectrum, a suppression of the inertial subrange can be observed along with an enhancement of the small scales. This is known to be caused by extraction of energy by the interfaces at large scales and the generation of small-scale motion due to coalescence events [78]. Vorticity is also known to align tangentially with the interfaces, leading to increased small-scale turbulence generation. The abnormality at the smallest scale can be attributed to the spurious velocities present near interfaces in the pseudopotential model.

When comparing the DNS spectrum with the high-resolution E-E LES spectra, we found a good agreement at the large and intermediate scales. Due to the absence of an interface, the above-mentioned additional mechanism is absent in the E-E model. Hence, the suppression of the large scales and the enhancement of the small scales are not observed. However, the presence of the second phase enhances the dissipation rate at the small scales, leading to good agreement at the large scales. Hence, the accuracy at the large scales is improved at the expense of accurate modeling the smaller scales. Both proposed models show very similar behavior, indicating good agreement.

Reducing the LES resolution to 64^3, Fig. 9 compares the averaged DNS emulsion spectrum with the LES spectrum obtained by using both the Poisson-based and the mixture-based model. Both models behave similarly, with the Poisson-based model being at a slightly better agreement with the DNS solution. Similarly to the high-resolution case, the large scales are well modeled by both models at the expense of the smallest scales. Both models can be concluded to provide good solutions with coarse grids. The lack of sharp interface-like gradients at steady state minimizes the error due to the lack of a density-dependent pressure in the mixture-based model, making it agree better with the Poisson-based model.

In this test case, the Poisson model was found to be about 7.8% slower than the mixture model. On the one hand, the mixture model requires the calculation of various correction terms in addition to the standard LB formulation which increases computation time. On the other hand, the simple wall-free geometry simulated here minimizes the number of iterations required for solving the Poisson equation. Therefore, for more complex flows, the Poisson model can be expected to be considerable slower than the mixture model. Given the significant efficiency improvements in using the mixture-based model, we can conclude that the latter is more suitable for cases without sharp gradients or extreme density ratios.

V. CONCLUSIONS

In this paper, we investigated the computational modeling of turbulent multiphase flows in an E-E LES approach exploiting the LB framework. Two lines of approach were developed to implement the E-E equations in LB with the correct pressure term in a robust and accurate manner. The first model used the pressure-free well-balanced approach to remove the pressure term from LB before reintroducing it as a force via a Poisson equation. The second approach adopted a mixture equation noniteratively generating the pressure, assuming an incompressible dilute mixture. This is then coupled with a full LB equation for the dispersed phase flow.

The Poisson-based approach reproduces the full E-E equations but can be computationally expensive due to the need to solve a Poisson equation. In contrast, the mixture-based model trades in some of the accuracy for lower computational costs. Both models use a modified drag force formulation that improves stability. Both these models are validated against two test cases: a falling cloud of particles and a Rayleigh Taylor instability. Both models were shown to match well with existing solutions in the literature. The mixture-based model exhibited higher errors near local density gradients because of the drawbacks of the incompressibility assumption used.

Subsequently, both models were used to conduct LESs of homogeneous isotropic turbulence in emulsions with the Smagorinsky SGS model. The results were compared with a DNS solution. Both models reproduced the larger scales of turbulence accurately. The DNS turbulence spectrum shows a deviation from the standard $5/3$ rule due to the presence of interfaces. Since this mechanism is not present in the E-E approach used, this deviation is not observed in our results. Hence, the E-E method accurately reproduced the large-scale flow at the expense of resolving the unique behavior at the smallest scales. Both methods were also shown to produce very identical results and exhibit good stability in the presence of complex turbulent flows.

ACKNOWLEDGMENTS

This research was conducted with the financial support of SSPC, the Taighde Éireann Research Centre for Pharmaceuticals, funded by Research Ireland and cofunded by the European Regional Development Fund, under Grant No. 12/RC/2275 P2.

DATA AVAILABILITY

The data that support the findings of this article are not publicly available upon publication because it is not technically feasible and/or the cost of preparing, depositing, and hosting the data would be prohibitive within the terms of this research project. The data are available from the authors upon reasonable request.

APPENDIX A: MIXTURE MODEL

This Appendix derives the mixture model from the constituent fluid equations. We begin with a general form of the two fluid equations, written as

$$\frac{\partial \rho_k \alpha_k}{\partial t} + \nabla(\rho_k \alpha_k \boldsymbol{u}_k) = 0, \tag{A1}$$

$$\frac{\partial(\rho_k \alpha_k \boldsymbol{u}_k)}{\partial t} + \nabla \cdot (\rho_k \alpha_k \boldsymbol{u}_k \boldsymbol{u}_k) = -\alpha_k \nabla P + \nabla \cdot \alpha_k \sigma_k + \rho_k \alpha_k \boldsymbol{g} + \boldsymbol{F}_k^{\text{drag}}, \tag{A2}$$

$$\sigma_k = \mu_k\big(\nabla \boldsymbol{u}_k + \nabla \boldsymbol{u}_k^T\big). \tag{A3}$$

To obtain a constitutive equation for the mixture of phases, the above set of equations can be added together as

$$\sum_k \frac{\partial \rho_k \alpha_k}{\partial t} + \sum_k \nabla(\rho_k \alpha_k \boldsymbol{u}_k) = 0, \tag{A4}$$

$$\sum_k \frac{\partial(\rho_k \alpha_k \boldsymbol{u}_k)}{\partial t} + \sum_k \nabla \cdot (\rho_k \alpha_k \boldsymbol{u}_k \boldsymbol{u}_k) = -\sum_k \alpha_k \nabla P + \sum_k \nabla \cdot \alpha_k \sigma_k + \sum_k \rho_k \alpha_k \boldsymbol{g} + \sum_k \boldsymbol{F}_k^{\text{drag}}. \tag{A5}$$

Moving the summation into the differential, we get

$$\frac{\partial \sum_k \rho_k \alpha_k}{\partial t} + \nabla\left(\sum_k \rho_k \alpha_k \boldsymbol{u}_k\right) = 0, \tag{A6}$$

$$\frac{\partial \sum_k (\rho_k \alpha_k \boldsymbol{u}_k)}{\partial t} + \nabla \cdot \left(\sum_k \rho_k \alpha_k \boldsymbol{u}_k \boldsymbol{u}_k\right) = -\sum_k \alpha_k \nabla P + \nabla \cdot \sum_k \alpha_k \sigma_k + \sum_k \rho_k \alpha_k \boldsymbol{g} + \sum_k \boldsymbol{F}_k^{\text{drag}}. \tag{A7}$$

We can define the mixture density and mixture velocity as

$$\rho_m = \sum_k \rho_k \alpha_k, \tag{A8}$$

$$\boldsymbol{u}_m = \frac{\sum_k \rho_k \alpha_k \boldsymbol{u}_k}{\rho_m}. \tag{A9}$$

Substituting Eqs. (A8) and (A9) into the continuity equation [Eq. (A6)], the mixture continuity equation can be obtained as

$$\frac{\partial \rho_m}{\partial t} + \nabla(\rho_m \boldsymbol{u}_m) = 0. \tag{A10}$$

Applying the same substitution to the momentum equation [Eq. (A7)], we get

$$\frac{\partial \rho_m \boldsymbol{u}_m}{\partial t} + \nabla \cdot \left(\sum_k \rho_k \alpha_k \boldsymbol{u}_k \boldsymbol{u}_k\right) = -\nabla P + \nabla \cdot \sum_k \alpha_k \sigma_k + \rho_m \boldsymbol{g}, \tag{A11}$$

where the drag forces of the various phases canceled out. Special care is needed for handling the convective and viscous dissipation terms in the above equation. Defining the diffusion velocity as $\boldsymbol{u}_{mk} = \boldsymbol{u}_k - \boldsymbol{u}_m$, the convective term can be rewritten as

$$\begin{aligned}
\nabla \cdot \left[\sum_k \rho_k \alpha_k \boldsymbol{u}_k \boldsymbol{u}_k\right] &= \nabla \cdot \left[\sum_k \rho_k \alpha_k (\boldsymbol{u}_m + \boldsymbol{u}_{mk})(\boldsymbol{u}_m + \boldsymbol{u}_{mk})\right] \\
&= \nabla \cdot \sum_k \rho_k \alpha_k \boldsymbol{u}_m \boldsymbol{u}_m + \nabla \cdot \sum_k \rho_k \alpha_k \boldsymbol{u}_{mk} \boldsymbol{u}_{mk} + 2\nabla \cdot \sum_k \rho_k \alpha_k \boldsymbol{u}_m \boldsymbol{u}_{mk} \\
&= \nabla \cdot (\rho_m \boldsymbol{u}_m \boldsymbol{u}_m) + \nabla \cdot \sum_k \rho_k \alpha_k \boldsymbol{u}_{mk} \boldsymbol{u}_{mk} + 2\nabla \cdot \sum_k \rho_k \alpha_k \boldsymbol{u}_m \boldsymbol{u}_{mk}.
\end{aligned} \tag{A12}$$

The last term in this equation can be shown to be zero as

$$\begin{aligned}
2\nabla \cdot \sum_k \rho_k \alpha_k \boldsymbol{u}_m \boldsymbol{u}_{mk} &= 2\nabla \cdot \left[\boldsymbol{u}_m \sum_k \rho_k \alpha_k (\boldsymbol{u}_k - \boldsymbol{u}_m)\right] \\
&= 2\nabla \cdot \left[\boldsymbol{u}_m \sum_k \rho_k \alpha_k \boldsymbol{u}_k - \boldsymbol{u}_m \boldsymbol{u}_m \sum_k \rho_k \alpha_k\right] \\
&= 2\nabla \cdot [\rho_m \boldsymbol{u}_m \boldsymbol{u}_m - \rho_m \boldsymbol{u}_m \boldsymbol{u}_m].
\end{aligned} \tag{A13}$$

Hence, the convective term becomes

$$\nabla \cdot \left[\sum_k \rho_k \alpha_k \boldsymbol{u}_k \boldsymbol{u}_k \right] = \nabla \cdot (\rho_m \boldsymbol{u}_m \boldsymbol{u}_m) + \nabla \cdot \sum_k \rho_k \alpha_k \boldsymbol{u}_{mk} \boldsymbol{u}_{mk}. \tag{A14}$$

Finally, the sum of the phase viscous terms is usually approximated as a mixture viscous term as

$$\nabla \cdot \sum_k \alpha_k \sigma_k \approx \nabla \cdot \sigma_m. \tag{A15}$$

This usually assumes a single velocity ($\boldsymbol{u}_k \approx \boldsymbol{u}_m$) which is valid for slower processes where the phase velocities are similar. However, the mixture model is often used in bubbly flows, where a significant slip velocity is observed, with satisfactory results. This discrepancy can be explained by reformulating the single velocity appproximation as a single velocity gradient assumption ($\nabla \cdot \boldsymbol{u}_k \approx \nabla \cdot \boldsymbol{u}_m$) which is less restrictive and results in the same set of equations.

Gathering the equations, the final mixture equations can be written as

$$\frac{\partial \rho_m \boldsymbol{u}_m}{\partial t} + \nabla \cdot (\rho_m \boldsymbol{u}_m \boldsymbol{u}_m) = -\nabla P + \nabla \cdot \sigma_m + \rho_m \boldsymbol{g} - \nabla \cdot \sum_k \rho_k \alpha_k \boldsymbol{u}_{mk} \boldsymbol{u}_{mk}. \tag{A16}$$

APPENDIX B: PHASE INTENSIVE MIXTURE MODEL

In this Appendix, the derivation of the phase intensive formulation of the mixture equations is presented. To begin, the mixture equation is written as

$$\frac{\partial}{\partial t}(\rho_m \mathbf{u}_m) + \nabla \cdot (\rho_m \mathbf{u}_m \mathbf{u}_m) = -\nabla P + \nabla \cdot \left[\mu_m \left(\nabla \boldsymbol{u}_m + \nabla \boldsymbol{u}_m^T \right) \right] + \mathbf{F}_m^C. \tag{B1}$$

Using the product rule on the left-hand side terms, we get

$$\begin{aligned} \frac{\partial}{\partial t}(\rho_m \mathbf{u}_m) + \nabla \cdot (\rho_m \mathbf{u}_m \mathbf{u}_m) &= \rho_m \frac{\partial \boldsymbol{u}_m}{\partial t} + \boldsymbol{u}_m \frac{\partial \rho_m}{\partial t} + \rho_m \nabla \cdot (\boldsymbol{u}_m \boldsymbol{u}_m) + \boldsymbol{u}_m \boldsymbol{u}_m \nabla \cdot \rho_m \\ &= \rho_m \frac{\partial \boldsymbol{u}_m}{\partial t} + \rho_m \nabla \cdot (\boldsymbol{u}_m \boldsymbol{u}_m) + \boldsymbol{u}_m \underbrace{\left[\frac{\partial \rho_m}{\partial t} + \boldsymbol{u}_m \nabla \cdot (\rho_m) \right]}_{0}. \end{aligned} \tag{B2}$$

The last term in the above equation is identical to the nonconservative form of the continuity equation, and thus is equal to zero.

Looking at the viscous term on the right-hand side, it can be reconstructed as

$$\begin{aligned} \nabla \cdot \left[\mu_m \left(\nabla \boldsymbol{u}_m + \nabla \boldsymbol{u}_m^T \right) \right] &= \nabla \cdot \left[\rho_m \nu_m \left(\nabla \boldsymbol{u}_m + \nabla \boldsymbol{u}_m^T \right) \right] \\ &= \rho_m \nabla \cdot \left[\nu_m \left(\nabla \boldsymbol{u}_m + \nabla \boldsymbol{u}_m^T \right) \right] + \nu_m \left(\nabla \boldsymbol{u}_m + \nabla \boldsymbol{u}_m^T \right) \nabla \rho_m. \end{aligned} \tag{B3}$$

Combining the terms and dividing by ρ_m, the phase intensive mixture equation becomes

$$\frac{\partial \boldsymbol{u}_m}{\partial t} + \nabla \cdot (\boldsymbol{u}_m \boldsymbol{u}_m) = -\frac{\nabla P}{\rho_m} + \nabla \cdot \left[\nu_m \left(\nabla \boldsymbol{u}_m + \nabla \boldsymbol{u}_m^T \right) \right] + \frac{\mathbf{F}_m^C}{\rho_m} + \nu_m \left(\nabla \boldsymbol{u}_m + \nabla \boldsymbol{u}_m^T \right) \frac{\nabla \rho_m}{\rho_m}. \tag{B4}$$

The last term forms a correction term denoted in the main text as $\mathbf{F}_{\mathrm{PI}}^C / \rho_m$.

[1] H. E. A. Van den Akker, The details of turbulent mixing process and their simulation, Adv. Chem. Eng. **31**, 151 (2006).

[2] Z. Guo and C. Shu, *Lattice Boltzmann Method and Its Applications in Engineering* (World Scientific, Singapore, 2013).

[3] J. G. Eggels and J. A. Somers, Numerical simulation of free convective flow using the lattice-Boltzmann scheme, Int. J. Heat Fluid Flow **16**, 357 (1995).

[4] J. Derksen and H. E. A. Van den Akker, Large eddy simulations on the flow driven by a Rushton turbine, AIChE J. **45**, 209 (1999).
[5] H. Hartmann, J. J. Derksen, C. Montavon, J. Pearson, I. S. Hamill, and H. E. A. Van den Akker, Assessment of large eddy and RANS stirred tank simulations by means of LDA, Chem. Eng. Sci. **59**, 2419 (2004).
[6] Y. Sato and K. Sekoguchi, Liquid velocity distribution in two-phase bubble flow, Int. J. Multiphase Flow **2**, 79 (1975).
[7] H. E. A. Van den Akker, Mesoscale flow structures and fluid–particle interactions, Adv. Chem. Eng. **46**, 281 (2015).
[8] P. Zhao, J. Xu, Q. Chang, W. Ge, and J. Wang, Euler-Lagrange simulation of dense gas-solid flow with local grid refinement, Powder Technol. **399**, 117199 (2022).
[9] R. Subburaj, Y. Tang, and N. G. Deen, Euler–Lagrange simulations of microstructured bubble columns using a novel cutting model, Ind. Eng. Chem. Res. **62**, 15656 (2023).
[10] P. Moin, Large eddy simulation of multi-phase turbulent flows in realistic combustors, Prog. Comput. Fluid Dyn. Int. J. **4**, 237 (2004).
[11] M. Ishii and T. Hibiki, *Thermo-fluid Dynamics of Two-phase Flow* (Springer, New York, NY, 2011), pp. 119–128.
[12] D. A. Drew, Mathematical modeling of two-phase flow, Annu. Rev. Fluid Mech. **15**, 261 (1983).
[13] J. Derksen, The lattice-Boltzmann method for multiphase fluid flow simulations and Euler-Lagrange large-eddy simulations, in *Multiphase Reacting Flows: Modelling and Simulation*, edited by D. L. Marchisio and R. O. Fox (Springer, Vienna, 2007), pp. 181–228.
[14] R. F. Mudde and H. E. A. Van Den Akker, 2D and 3D simulations of an internal airlift loop reactor on the basis of a two-fluid model, Chem. Eng. Sci. **56**, 6351 (2001).
[15] R. S. Oey, R. F. Mudde, L. M. Portela, and H. E. A. Van Den Akker, Simulation of a slurry airlift using a two-fluid model, Chem. Eng. Sci. **56**, 673 (2001).
[16] R. S. Oey, R. F. Mudde, and H. E. A. Van den Akker, Sensitivity study on interfacial closure laws in two-fluid bubbly flow simulations, AIChE J. **49**, 1621 (2003).
[17] R. Jamshidian, J. Scully, and H. E. A. Van den Akker, Two-fluid simulations of an aerated lab-scale bioreactor, Chem. Eng. Res. Des. **196**, 254 (2023).
[18] R. Jamshidian, J. Scully, and H. E. A. Van den Akker, A computational fluid dynamics study of mass transfer in a large-scale aerated stirred bioreactor, Chem. Eng. J. **509**, 160723 (2025).
[19] N. G. Deen, T. Solberg, and B. H. Hjertager, Large eddy simulation of the gas–liquid flow in a square cross-sectioned bubble column, Chem. Eng. Sci. **56**, 6341 (2001).
[20] B. Ničeno, M. Boucker, and B. L. Smith, Euler-Euler large eddy simulation of a square cross-sectional bubble column using the Neptune_CFD code, Sci. Technol. Nucl. Install. **2009**, 410272 (2009).
[21] T. Ma, T. Ziegenhein, D. Lucas, E. Krepper, and J. Fröhlich, Euler–Euler large eddy simulations for dispersed turbulent bubbly flows, Int. J. Heat Fluid Flow **56**, 51 (2015).
[22] M. G. Fard, Y. Stiriba, B. Gourich, C. Vial, and F. X. Grau, Euler-Euler large eddy simulations of the gas–liquid flow in a cylindrical bubble column, Nucl. Eng. Des. **369**, 110823 (2020).
[23] M. T. Dhotre, B. Niceno, and B. L. Smith, Large eddy simulation of a bubble column using dynamic sub-grid scale model, Chem. Eng. J. **136**, 337 (2008).
[24] D. Papoulias, M. Tandon, A. Splawski, and S. Lo, Eulerian-Eulerian large-eddy simulations in bubble-columns, Notes Numer. Fluid Mech. Multidisc. Design **135**, 199 (2018).
[25] H. E. A. Van den Akker, The Euler-Euler approach to dispersed two-phase flows in the turbulent regime, ERCOFTAC Bull. **36**, 30 (1998).
[26] S. Long, J. Yang, X. Huang, G. Li, W. Shi, M. Sommerfeld, and X. Yang, Large-eddy simulation of gas–liquid two-phase flow in a bubble column reactor using a modified sub-grid scale model with the consideration of bubble-eddy interaction, Int. J. Heat Mass Transf. **161**, 120240 (2020).
[27] S. Long, X. Yang, J. Yang, M. Sommerfeld, and C. Xue, Large eddy simulation of bubble column bubbly flow considering subgrid-scale turbulent diffusion effects and bubble oscillation, Chem. Eng. Technol. **46**, 1791 (2023).

[28] B. Blais, J.-M. Tucny, D. Vidal, and F. Bertrand, A conservative lattice Boltzmann model for the volume-averaged Navier-Stokes equations based on a novel collision operator, J. Comput. Phys. **294**, 258 (2015).
[29] T. Wang and J. Wang, Two-fluid model based on the lattice Boltzmann equation, Phys. Rev. E **71**, 045301(R) (2005).
[30] J. Zhang, L. Wang, and J. Ouyang, Lattice Boltzmann model for the volume-averaged Navier-Stokes equations, Europhys. Lett. **107**, 20001 (2014).
[31] S. B. Höcker, R. Trunk, W. Dörfler, and M. J. Krause, Towards the simulations of inertial dense particulate flows with a volume-averaged lattice Boltzmann method, Comput. Fluids **166**, 152 (2018).
[32] Z. Guo, Well-balanced lattice Boltzmann model for two-phase systems, Phys. Fluids **33**, 031709 (2021).
[33] T. Inamuro, T. Ogata, S. Tajima, and N. Konishi, A lattice Boltzmann method for incompressible two-phase flows with large density differences, J. Comput. Phys. **198**, 628 (2004).
[34] S. Shu, J. Zhang, and N. Yang, GPU-accelerated transient lattice Boltzmann simulation of bubble column reactors, Chem. Eng. Sci. **214**, 115436 (2020).
[35] M. Manninen, V. Taivassalo, and S. Kallio, *On the Mixture Model for Multiphase Flow*, VTT Publications No. 288 (VTT Technical Research Centre of Finland, Finland, 1996).
[36] P. L. Bhatnagar, E. P. Gross, and M. Krook, A model for collision processes in gases. I. Small amplitude processes in charged and neutral one-component systems, Phys. Rev. **94**, 511 (1954).
[37] T. Krüger, H. Kusumaatmaja, A. Kuzmin, O. Shardt, G. Silva, and E. M. Viggen, Forces, in *The Lattice Boltzmann Method*, Graduate Texts in Physics (Springer, Cham, 2017).
[38] X. Shan and H. Chen, Lattice Boltzmann model for simulating flows with multiple phases and components, Phys. Rev. E **47**, 1815 (1993).
[39] K. Rietema and H. E. A. Van den Akker, On the momentum equations in dispersed two-phase systems, Int. J. Multiphase Flow **9**, 21 (1983).
[40] F. Song, W. Wang, and J. Li, A lattice Boltzmann method for particle-fluid two-phase flow, Chem. Eng. Sci. **102**, 442 (2013).
[41] P. J. Oliveira and R. I. Issa, Numerical aspects of an algorithm for the Eulerian simulation of two-phase flows, Int. J. Numer. Methods Fluids **43**, 1177 (2003).
[42] L. Silva and P. Lage, Development and implementation of a polydispersed multiphase flow model in OpenFOAM, Comput. Chem. Eng. **35**, 2653 (2011).
[43] H. Rusche, Computational fluid dynamics of dispersed two-phase flows at high phase fractions, Ph.D. thesis, Imperial College London, 2002, p. 335.
[44] R. Keser, V. Vukčević, M. Battistoni, H. Im, and H. Jasak, Implicitly coupled phase fraction equations for the Eulerian multi-fluid model, Comput. Fluids **192**, 104277 (2019).
[45] G. G. Ferreira, P. L. Lage, L. F. L. Silva, and H. Jasak, Implementation of an implicit pressure–velocity coupling for the Eulerian multi-fluid model, Comput. Fluids **181**, 188 (2019).
[46] X. He and L. S. Luo, Lattice Boltzmann model for the incompressible Navier-Stokes equation, J. Stat. Phys. **88**, 927 (1997).
[47] Z. Guo, B. Shi, and N. Wang, Lattice BGK model for incompressible Navier-Stokes equation, J. Comput. Phys. **165**, 288 (2000).
[48] R. Du, B. Shi, and X. Chen, Multi-relaxation-time lattice Boltzmann model for incompressible flow, Phys. Lett. A **359**, 564 (2006).
[49] R. Du and B. C. Shi, Incompressible multi-relaxation-time lattice Boltzmann model in 3-D space, J. Hydrodyn. **22**, 782 (2010).
[50] J. Sanyal, S. Vásquez, S. Roy, and M. Dudukovic, Numerical simulation of gas–liquid dynamics in cylindrical bubble column reactors, Chem. Eng. Sci. **54**, 5071 (1999).
[51] L. Schiller and A. Maumann, Über die grundlegenden berechnungen bei der schwerkraftaufbereitung, Z. Ver. Dtsch. Ing. **77**, 318 (1933).
[52] X. Shan and H. Chen, Simulation of nonideal gases and liquid-gas phase transitions by the lattice Boltzmann equation, Phys. Rev. E **49**, 2941 (1994).
[53] V. Heidler, O. Bublík, A. Pecka, and J. Vimmr, Eulerian–Lagrangian and Eulerian–Eulerian approaches for the simulation of particle-laden free surface flows using the lattice Boltzmann method, J. Comput. Appl. Math. **398**, 113672 (2021).

[54] I. M. Krieger and T. J. Dougherty, A mechanism for non-Newtonian flow in suspensions of rigid spheres, Trans. Soc. Rheol. **3**, 137 (1959).
[55] Rayleigh, Investigation of the character of the equilibrium of an incompressible heavy fluid of variable density, Proc. London Math. Soc. **s1-14**, 170 (1882).
[56] G. I. Taylor, The instability of liquid surfaces when accelerated in a direction perpendicular to their planes. I, Proc. R. Soc. Lond. A **201**, 192 (1950).
[57] J. Kilkenny, S. Glendinning, S. Haan, B. Hammel, J. Lindl, D. Munro, B. Remington, S. Weber, J. Knauer, and C. Verdon, A review of the ablative stabilization of the Rayleigh-Taylor instability in regimes relevant to inertial confinement fusion, Phys. Plasmas **1**, 1379 (1994).
[58] M. Livio, J. R. Buchler, and S. A. Colgate, Rayleigh-Taylor driven SN explosions: A two-dimensional numerical study, Astrophys. J. **238**, L139 (1980).
[59] J. A. Whitehead Jr. and D. S. Luther, Dynamics of laboratory diapir and plume models, J. Geophys. Res. **80**, 705 (1975).
[60] H. Liang, Q. X. Li, B. C. Shi, and Z. H. Chai, Lattice Boltzmann simulation of three-dimensional Rayleigh-Taylor instability, Phys. Rev. E **93**, 033113 (2016).
[61] H. G. Lee and J. Kim, Numerical simulation of the three-dimensional Rayleigh-Taylor instability, Comput. Math. Appl. **66**, 1466 (2013).
[62] V. B. Rozanov, P. A. Kuchugov, N. V. Zmitrenko, and Y. V. Yanilkin, Effect of initial conditions on the development of Rayleigh–Taylor instability, J. Russ. Laser Res. **36**, 139 (2015).
[63] D. Sharp, An overview of Rayleigh-Taylor instability, Physica D **12**, 3 (1984).
[64] J. Smagorinsky, General circulation experiments with the primitive equations, Mon. Weather Rev. **91**, 99 (1963).
[65] P. J. Mason and N. S. Callen, On the magnitude of the subgrid-scale eddy coefficient in large-eddy simulations of turbulent channel flow, J. Fluid Mech. **162**, 439 (1986).
[66] K. Hutter, Y. Wang, and I. P. Chubarenko, Subgrid-scale parameterization in numerical simulations of lake circulation, in *Physics of Lakes: Volume 3: Methods of Understanding Lakes as Components of the Geophysical Environment* (Springer International Publishing, Cham, 2014), pp. 173–205.
[67] N. N. Mansour, P. Moin, W. C. Reynolds, and J. H. Ferziger, Improved methods for large eddy simulations of turbulence, in *Turbulent Shear Flows I*, edited by F. Durst, B. E. Launder, F. W. Schmidt, and J. H. Whitelaw (Springer, Berlin, Heidelberg, 1979), pp. 386–401.
[68] J. W. Deardorff, A numerical study of three-dimensional turbulent channel flow at large Reynolds numbers, J. Fluid Mech. **41**, 453 (1970).
[69] J. J. Giacomelli and H. E. A. Van den Akker, Time scales and turbulent spectra above the base of stirred vessels from large eddy simulations, Flow, Turbul. Combust. **105**, 31 (2020).
[70] G. T. Zachariah and H. E. A. Van den Akker, Representing the small scales of turbulence by periodic box homogeneous isotropic turbulence simulations, Flow, Turbul. Combust. **111**, 1101 (2023).
[71] M. Germano, U. Piomelli, P. Moin, and W. H. Cabot, A dynamic subgrid-scale eddy viscosity model, Phys. Fluids **3**, 1760 (1991).
[72] M. Germano, Turbulence: The filtering approach, J. Fluid Mech. **238**, 325 (1992).
[73] K. N. Premnath, M. J. Pattison, and S. Banerjee, Dynamic subgrid scale modeling of turbulent flows using lattice-Boltzmann method, Physica A **388**, 2640 (2009).
[74] Y.-H. Dong, P. Sagaut, and S. Marie, Inertial consistent subgrid model for large-eddy simulation based on the lattice Boltzmann method, Phys. Fluids **20**, 035104 (2008).
[75] M. Weickert, G. Teike, O. Schmidt, and M. Sommerfeld, Investigation of the LES WALE turbulence model within the lattice Boltzmann framework, Comput. Math. Appl. **59**, 2200 (2010).
[76] S. Hou, J. Sterling, S. Chen, and G. Doolen, A lattice Boltzmann subgrid model for high Reynolds number flows, in *Pattern Formation and Lattice Gas Automata*, edited by A. T. Lawniczak and R. Kapral, Fields Institute Communications Vol. 6 (American Mathematical Society, Providence, RI, 1996), pp. 151–166.
[77] X. Yu, X. Tang, W. Wang, F. Wang, Z. Chen, and X. Shi, A lattice Boltzmann model coupled with a large eddy simulation model for flows around a groyne, Int. J. Sediment Res. **25**, 271 (2010).
[78] S. Mukherjee, A. Safdari, O. Shardt, S. Kenjereš, and H. E. A. Van Den Akker, Droplet-turbulence interactions and quasi-equilibrium dynamics in turbulent emulsions, J. Fluid Mech. **878**, 221 (2019).